Signals Correlation Algorithms For Cheaper Surveys: Using Windowing Functions.

M. T. Atemkeng[1], O. M. Smirnov[12]*, C. Tasse[123], G. Foster[12], J. Jonas[12]

[1]*Department of Physics and Electronics, Rhodes University, PO Box 94, Grahamstown, 6140, South Africa*
[2]*SKA South Africa, 3rd Floor, The Park, Park Road, Pinelands, 7405, South Africa*
[3]*GEPI, Observatoire de Paris, CNRS, Universite Paris Diderot, 5 place Jules Janssen, 92190 Meudon, France*

ABSTRACT

This paper investigates the use of baseline dependent windowing functions in interferometry data to minimize the loss of signal amplitude (smearing) when the correlated data is averaged over wide bandwidth and long time. In radio interferometry smearing is reduced when a cross-correlator averages the correlated data over narrower bandwidth and shorter integration times. Unfortunately, this leads to a huge amount of data to manage and it is becoming a bottleneck for further data processing such as calibration and imaging. With future generation surveys, it is important to investigate the reduction of the output data rate. Therefore, the focus of this paper is on the use of baselines dependent windowing functions to keep smearing down at an acceptable extent and at the same time significantly suppress signals from out field of view sources, while the nominal sensitivity is conserved.

Key words: Instrumentation: interferometers, Methods: data analysis, Methods: numerical, Techniques: interferometric

1 INTRODUCTION

The recent radio astronomy techniques is to build a single, gigantic instrument called *interferometer*, from the combination of several small parabolic antennas separated over kilometres (**?**). The signal from each antenna is combined at the level of a cross-correlator to form the interferometer data output. The cross-correlator carries out data reduction and filters out an amount of noise by averaging the signal of each baseline over discrete time and/or frequency bins. It is well known in interferometry that averaging can lead to the loss of signal amplitude when the cross correlator integrate over a longer period of time and a wider bandwidth. This effect is known as time-average smearing and bandwidth smearing (Thompson *et al.* **?**). The above effects cause the distortion of sources within the field of interest by decreasing their intensity.

To keep smearing down at acceptable levels, a correlator must cross-correlate the signal over a shorter period of time and a narrower bandwidth, hence producing a large amount of data for subsequence stage such as imaging (Martí-Vidal & Marcaide 2008; Linfield 1986), calibration (**?**), etc. This huge amount of data is becoming an increasingly serious problem and becoming more challenging as the computational demands of the next generation radio telescopes will rise significantly (see the SKA phase 1 specification **?**). Similarly, the next generation of radio telescopes will require an unprecedented level of SNR while mapping large regions of the sky. Thus, a substantial increase in *SNR* can only be achieve by observing for longer time at wider bandwidth without loss of signal: this is not realisable with averaging. Therefore, it becomes urgent to develop new decorrelation algorithm techniques that will allow the required SNR of the future radio telescopes.

In this paper, we investigate the efficiency of correlator windowing functions for the reduction of interferometric data and the recovery of interferometers arrays desire FoV, with the ultimate goal of reaching higher SNR. The main idea is to achieve a high SNR by conserving the astrophysical signal and by limiting the noise. Thermal noise can be driven arbitrary low by increasing the observing time[1], but in radio astronomy confusion noise is a major problem and can even cause calibration to fail. Therefore, we seek to use a windowing function that will conserve the useful signal while also limiting sidelobes confusion from out of FoV sources.

$$SNR = \frac{S_{use}}{N_{ter} + N_{con}} \tag{1}$$

* E-mail: o.smirnov@ru.ac.za (OMS); m.atemkeng@gmail.com (MTA); cyril.tasse@obspm.fr (CT); griffin.foster@gmail.com (GF); j.jonas@ru.ac.za (JJ)

[1] ...

● "*Useful signal*", S_{use} the signal from source in the field of interest. These sources should be accurately recovered over the instrument entire FoV : correlator windowing functions maximized this signal by allowing the interferometer array to map a large region of the sky.

● "*Sidelobe confusion*", N_{con} signal from out field of view sources received from their sidelobes. These sources are not of interest and should be removed : correlator windowing functions acts as a remover of these signals when the array is mapping a large region of the sky.

● "*Thermal noise*", N_{ter} the thermal noise from the instrument, ionosphere, etc. Averaging presents theoretically a maximum sensitivity, but the use of extended correlator windowing functions can reduce or eliminate the loss of the nominal sensitivity.

The proposed techniques are applied to MeerKAT (Karoo Array Telescope) **?** and the Very Large Array (VLA)**?** and could also be used for future radio telescopes such as the SKA.

2   OVERVIEWS AND DEFINITIONS

2.1   Visibility and relation with the sky

An interferometer array measured a quantity $V = V(u, v, w)$ known classically as the visibility function (see **?**). The variables u, v and w are in unit of wavelength and they are the coordinates of the vector of which the norm is the distance between two antennas, known in interferometry as a baseline. A source in the sky will see u and v oriented towards the direction East-West and South-North respectively and w is directed towards the phase centre of the source plane or image plane. The projection of u and v in the image plane are l and m respectively. They are the observed source coordinates, measured in radian. The ideal measurement of interferometric wide-field imaging also known as the van Cittert-Zernike theorem (Thompson *et al*. 2001, Eq.6) is given by

$$V_{pq} = \int \int \frac{I(l,m)}{\sqrt{1-l^2-m^2}} e^{-2\pi i \phi(u,v,w)} dl dm, \qquad (2)$$

where $I(l,m)$ is the sky brightness and $\phi(u, v, w) = u.l + v.m + w.(\sqrt{1-l^2-m^2}-1)$ is a term from the cross-correlator that models the direction in the sky and the separation of the two antennas. The term $\sqrt{1-l^2-m^2}$ is the result of the projection of the celestial sphere on the image plane.

2.2   Averaging and convolution

The Earth rotation causes the phase, $\phi(u,v,w)$ to variate in time. The baseline coordinates are defined in units of wavelength, and making $\phi(u,v,w)$ to variate in frequency. To take this effect into account, Eq. 2 is rewritten as an integration over time and frequency interval. If we consider that $[t_s, t_e]$ is the time integration interval and $[\nu_s, \nu_e]$ the frequency integration interval, then Eq.2 can be rewritten as:

$$V_{pq,(t_c,\nu_c)}^{corr} = \frac{1}{\Delta t \Delta \nu} \int_{t_c-dt/2}^{t_c+dt/2} \int_{\nu_c-d\nu/2}^{\nu_c+d\nu/2} V_{pq,(t,\nu)} d\nu dt. \qquad (3)$$

Here, $V_{pq,(t,\nu)}$ is a continuous function, in reality we know only the sampled visibility, $V_{pq,(t,\nu)}^{samp} = S_{pq,(t,\nu)} V_{pq,(t,\nu)}$ at a specific time and frequency, where $S_{pq,(t,\nu)}$ is a sampling function that indicates where the (u, v) data for the baseline (p, q) are measured during the time and frequency integration. Therefore, Eq.3 holds for many sources, when the signal at the centre frequency and at the centre time is restricted to a narrow frequency interval and to a short time interval, this is the current efficient observing mode. However, the mathematics behind is as follows:

$$V_{pq,(t_c,\nu_c)}^{corr} = \frac{1}{n_t n_\nu} \sum_{i=1}^{n_t} \sum_{j=1}^{n_\nu} V_{pq,(t,\nu)}^{samp}. \qquad (4)$$

Here, n_t and n_ν are the number of discrete times within the time interval and the number of discrete frequency within the frequency interval respectively. For convenience, lets introduce a normalized *Boxcar* windowing function, $\Pi_{pq,(t_c-t,\nu_c-\nu)}$ that will attribute an equal weight (in this case $1/n_t n_\nu$) to all sampling visibilities points. We can therefore rewrite Eq. 4 as:

$$V_{pq,(t_c,\nu_c)}^{corr} = \sum_{i=1}^{n_t} \sum_{j=1}^{n_\nu} \Pi_{pq,(t_c-t_i,\nu_c-\nu_j)} V_{pq,(t_i,\nu_j)}^{samp}. \qquad (5)$$

It is worth noting that Eq.5 is a naturally weighted visibility and is a two dimensional convolution between the *Boxcar* windowing function and the sampled visibility. Thus, averaging is equivalent to convolving the sampled visibility with a *Boxcar* windowing function. Mathematically, this is described as follows:

$$V_{pq,(t_c,\nu_c)}^{corr} = c_{pq,(t,\nu)} \cdot \left(\left(\Pi_{pq} \circ V_{pq}^{samp} \right)_{(t,\nu)} \right). \qquad (6)$$

Here, $c_{pq,(t,\nu)}$ is a function that samples the result of $\left(\Pi_{pq} \circ V_{pq}^{samp} \right)_{(t,\nu)}$ at the centre time interval and centre frequency interval.

2.3   Effect of time and bandwidth averaging

During imaging (Martí-Vidal & Marcaide 2008), Eq.6 is inverse Fourier transform, and the convolution theorem is applied, the *sinc* function therefore multiply the sky (see appendixB for a short discussion and illustration). Thus, the sky map is tapered by the *sinc* function in the l and m direction, the response is maximal for sources at the phase centre ($l = 0, m = 0$), while for off-phase centre sources, the response is smeared (decreased) for larger Δt and $\Delta \nu$. The Fourier phase components $2\pi \phi(u, v, w)$ is a function of the direction in the sky, the wavelength, the separation of antennas as well as the integration time and frequency. Therefore, a maximal phase will occurs on longer baselines while a small phase on shorter baselines. Thus, this explained while the degree of smearing increases with the position of a source and the baseline length (see Thompson *et al*.)

● Fig.1 shows the attenuation of a source at various coordinates in the sky for various integration time interval. More than 90% of the source brightness is measured for integration less than or equal to $25s$ when this source is within $[0°, 3°]$. We can noticed on this figure that, we could not

maintained the 90% of the source brightness within $[0°, 1°]$ if the desire FoV is $2°$ and suppressed the source within $[1°, 3°]$ with these short integration. Therefore, as mention earlier in this work, a small integration produced large data and maintained sidelobes contamination from out field of view sources.

- Fig.**??** shows the attenuation of a source at various coordinates in the sky for various integration time interval. More than 90% of the source brightness is measured for integration less than or equal to $25s$ when this source is within $[0°, 3°]$. We can noticed on this figure that, we could not maintained the 90% of the source brightness within $[0°, 1°]$ if the desire FoV is $2°$ and suppressed the source within $[1°, 3°]$ with these short integration. Therefore, as mention earlier in this work, a small integration produced large data and maintained sidelobes contamination from out field of view sources

Fortunately, since the response is maximal only for sources at the phase centre, an interesting approach is achieved by convolving the observed visibility with a windowing function that depends on (u, v) coordinates spacing (baseline dependent windowing function). However, a windowing function with a wide dynamic range spectrum is preferable in this work.

2.4 Imaging

Recall from the previous section that, the boxcar windowing function can be replaced by a windowing function, $W_{pq,(t,\nu)}$ that depends on (u, v) spacing. Now, consider that $W_{pq,(t,\nu)}$ is a $n_t \times n_\nu$ matrix of elements $W_{pq,(t_i,\nu_j)}|_{i=1,n_t}^{j=1,n_\nu}$, the weights of (u, v) points. From the full sky Radio Interferometry Measurement Equation (RIME) formalism (see Hamaka et *al*, O.M. Smirnov (2010a)), the sampled visibilities can be presented mathematically as a $4 \times n_t \times n_\nu$ matrix of four polarizations time and frequency dependent matrices each of size $n_t \times n_\nu$.

$$\mathbf{V}_{pq,(t,\nu)}^{samp} = \left(\mathbf{V}_{pq,(t,\nu)}^0, \mathbf{V}_{pq,(t,\nu)}^1, \mathbf{V}_{pq,(t,\nu)}^2, \mathbf{V}_{pq,(t,\nu)}^3 \right)^T.$$

The convolution operator is linear, therefore we can rewrite Eq.6 in terms of a series of linear transformations or functional model as:

$$V_{pq,(t_c,\nu_c)}^{corr} = \mathbf{C}_{pq,(t,\nu)}^{block} \cdot \mathbf{W}_{pq,(t,\nu)}^{block} \cdot \mathbf{V}_{pq,(t,\nu)}^{samp}. \quad (7)$$

Here, $\mathbf{C}_{pq,(t,\nu)}^{block}$ and $\mathbf{W}_{pq,(t,\nu)}^{block}$ are blocks diagonals matrices of size $(4n_t n_\nu) \times (4n_t n_\nu)$, the block elements are $\mathbf{W}_{pq,(t,\nu)}$ and $\mathbf{C}_{pq,(t,\nu)}$ respectively, where $\mathbf{C}_{pq,(t,\nu)}$ is the centre time interval and centre frequency interval sampling matrix of size $n_t \times n_\nu$. This is the result of the time and frequency integration for the baseline (p, q). For a synthesis, the baseline (p, q) made a full coverage in the (u, v) plane. Therefore, we can package into a single matrix, $\mathbf{V}_{pq,(t',\nu')}^{corr}$ of size $(4N_t N_\nu) \times (4N_t N_\nu)$ the weighted average visibilities of the baseline (p, q) during the synthesis as follows:

$$\mathbf{V}_{pq,(t',\nu')}^{corr} = \mathbf{C}_{pq,(t,\nu)}^{block,n} \cdot \mathbf{W}_{pq,(t,\nu)}^{block,n} \cdot \mathbf{V}_{pq,(t,\nu)}^{samp,n}, \quad (8)$$

where N_t and N_ν are the number of time sample and frequency channels entering the Fourier domain. If the synthe-

sis time is T and the frequency range is F, then $T = N_t \times \Delta t$ and $F = N_\nu \times \Delta \nu$. The the size of $\mathbf{V}_{pq,(t',\nu')}^{corr}$ can also be written as $(4N_\nu^{pq}) \times (4N_\nu^{pq})$, where N_ν^{pq} is the number of time and frequency visibilities for the baseline (p, q). The matrices $\mathbf{C}_{pq,(t,\nu)}^{block,n}$ and $\mathbf{W}_{pq,(t,\nu)}^{block,n}$ are diagonals blocks matrices of size $(4N_\nu^{pq} n_t n_\nu) \times (4N_\nu^{pq} n_t n_\nu)$ where each diagonal block is the block diagonal matrix $\mathbf{C}_{pq,(t,\nu)}^{block}$ and $\mathbf{W}_{pq,(t,\nu)}^{block}$ respectively. n is the number of blocks elements. The sampled visibilities $\mathbf{V}_{pq,(t,\nu)}^{samp,n} = \mathbf{S}_{pq,(t,\nu)}^n \cdot \mathbf{V}_{pq,(t,\nu)}^n$ is a one row matrix of size $(N_\nu^{pq} 4n_t n_\nu) \times (4n_t n_\nu)$ made of $\mathbf{V}_{pq,(t,\nu)}^{samp}$ on top of each other and the matrix $\mathbf{S}_{pq,(t,\nu)}^n$ is the (u, v) plane sampling function for the visibilities $\mathbf{V}_{pq,(t,\nu)}^n$ of size $(N_\nu^{pq} 4n_t n_\nu) \times (4n_t n_\nu)$. We can write:

$$\mathbf{V}_{pq,(t'\nu')}^{corr} = \mathbf{C}_{pq,(t,\nu)}^{block,n} \cdot \mathbf{W}_{pq,(t,\nu)}^{block,n} \cdot \mathbf{S}_{pq,(t,\nu)}^n \mathbf{F} \cdot \mathcal{I}_{l,m}^{sky}, \quad (9)$$

if the number of pixel in the sky model is N_{pix}, then the true sky image vector $\mathcal{I}_{l,m}^{sky}$ has a size of $4N_{pix}$ and $\mathbf{F}$ is a block diagonal Fourier transform operator of size $(4N_{pix}) \times (4N_{pix})$.

We are generally interested in using the total set of visibilities over baselines, time and frequencies, having $4 \times N_\nu$ visibilities measured over all baselines and $N_\nu = n_{bl} \times N_\nu^{pq}$ in this case. Here, n_{bl} is the number of baseline. We then have:

$$\mathbf{V}_{array,(t',\nu')}^{corr} = \mathbf{A} \cdot \mathcal{I}_{l,m}^{sky} + \epsilon. \quad (10)$$

Here, ϵ is the random error component or noise and $\mathbf{A}$ is the design matrix of size $(4N_\nu) \times (4N_{pix})$ corresponding to N_ν visibilities weights, defined as

$$\mathbf{A} = \begin{bmatrix} \mathbf{C}_{(t,\nu)}^{block,n} \cdot \mathbf{W}_{01,(t,\nu)}^{block,n} \cdot \mathbf{S}_{01,(t,\nu)}^n \cdot \mathbf{F} \\ \vdots \\ \mathbf{C}_{(t,\nu)}^{block,n} \cdot \mathbf{W}_{ik,(t,\nu)}^{block,n} \cdot \mathbf{S}_{ik,(t,\nu)}^n \cdot \mathbf{F} \\ \vdots \\ \mathbf{C}_{(t,\nu)}^{block,n} \cdot \mathbf{W}_{jl,(t,\nu)}^{block,n} \cdot \mathbf{S}_{jl,(t,\nu)}^n \cdot \mathbf{F} \end{bmatrix}$$

The dirty image, $\mathcal{I}_{l,m}^D$ of size $4N_{pix}$ can then be derived as follow:

$$\mathcal{I}_{l,m}^D = \mathbf{F}^H \cdot \mathbf{A} \cdot \mathcal{I}_{l,m}^{sky} + \epsilon. \quad (11)$$

Here, H represents the the conjugate transpose operation also known as a Hermitian transpose and $\mathbf{F}^H$ is a block diagonal inverse Fourier transform operator of size $(4N_{pix}) \times (4N_{pix})$. The estimate of ϵ, for the map centre pixel is given by:

$$\begin{aligned} \widetilde{\epsilon}_{o,o} &= \widetilde{\mathcal{I}}_{o,o} - \mathbf{F}^H \cdot \mathbf{A} \cdot \widetilde{\mathcal{I}}_{o,o} \\ &= \frac{1}{N_\nu} \sum_{k=1}^{N_\nu^{pq}} \left\{ \mathbf{A} \cdot V_{array,(t,\nu)}^n - \mathbf{F}^H \cdot \mathbf{A}^2 \cdot V_{array,(t,\nu)}^n \right\}. \end{aligned}$$

Here, $V_{array,(t,\nu)}^n$ is a one row matrix of size $(N_\nu 4n_t n_\nu) \times (4n_t n_\nu)$ made of $\mathbf{V}_{pq,(t,\nu)}^n$ on top of each other.
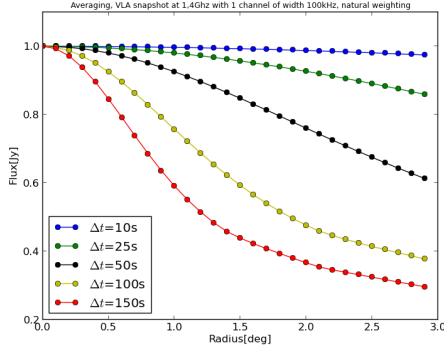
Figure 1. The fall of the intensity of a 1Jy source move from the phase centre for Δt integration synthesis at 100KHz bandwidth.
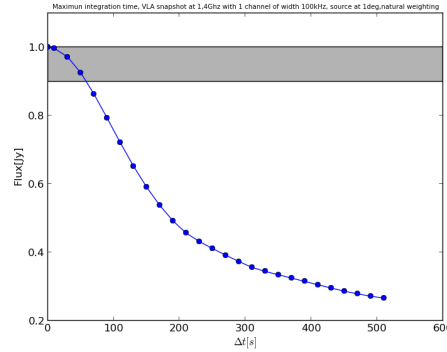
Figure 2. (b)Response to a 1Jy source at 1deg, as a function of Δt with 100KHz bandwidth

3 DERIVATION OF BDWF: FOV SIGNALS RECOVERY

3.1 Description

Missing spaces between sampled (u, v) coordinates has an important dependences on the baseline length. However, the spacing between longer baselines (u, v) coordinates are wider then the one on shorter baselines, this is the obvious effect that explained while sources are more distorted on longer baselines compare to shorter one. Therefore, if one have to attribute a (u, v) weight, it may be as a function of the baseline length, in such a way that the distortion rate is taken into account over baselines. We aims in this section, to describe an algorithm that we used with a baseline-dependent windowing function to assign a proper weight to a data reference by a (u, v) coordinate considering the *spacing*[2] between the baseline (u, v) coordinates.

Fig.3 shows a snapshot coverage of an integration interval. For shorter baselines, the tracks are closer to the centre of rotation and for longer baselines the tracks are farther away from this centre. The *dot marks* are the data for a sampled (u, v) data, and the arrows indicates the separation between (u, v) coordinates and the centre (u, v) coordinate. It is trivial to see on this figure that these separations are wider on longer baselines. The results of averaging is assigned to the centre (u, v) coordinate coloured in red.

3.2 Methods

Depending on the arrays, we show here that we can use the fact that, the spacing of long baselines (u, v) coordinates are wider and design a high dynamic range filter on longer baseline that will recover the desire FoV of the interferometer, and at the same time reducing the data rate. During an integration, the Earth rotation makes baselines coordinates u and v to variates in time and frequency. We can therefore package the (u, v) coordinates changes and the frequency changes of a baseline pq into a single matrix of size $n_t \times 2$

and into a single vector of dimension n_v respectively.

$$\mathbf{U}_{pq,t} = \left(\mathbf{u}_{pq,t_s}, \ldots, \mathbf{u}_{pq,t_c}, \ldots, \mathbf{u}_{pq,t_e} \right)^T$$

$$\boldsymbol{v} = \left(v_s, \ldots, v_c, \ldots, v_e \right)^T$$

where the indexes s, c and e references the integration interval starting, centre, and ending time respectively and T the transpose operator. The elements of $\mathbf{U}_{pq,t}$ are functions of time and frequency representing a (u, v) coordinate. We defined the function, $\overline{\overline{\cdot}}$ on a $n_t \times 2$ matrix as follow:

$$\overline{\overline{\mathbf{U}}}_{pq,t} = \left(||\mathbf{u}_{pq,t_s}||, \ldots, ||\mathbf{u}_{pq,t_c}||, \ldots, ||\mathbf{u}_{pq,t_e}|| \right)^T, \quad (12)$$

where $||.||$ is the Euclidean norm.

Definition 1.1. (Time direction spacing) The matrix that model the spacing between the (u, v) coordinates and the centre (u, v) coordinate of a baseline (p, q) across the time direction is defined as

$$\mathbf{U}^s_{pq,t} = \frac{v_c}{c} \cdot \left\{ \mathbf{U}_{pq,t} - \mathbf{H}_{pq,t} \right\},$$

where c is the speed of the light and $\mathbf{H}_{pq}$ is a matrix of size $n_t \times 2$ that model the centre uv-coordinate, $\mathbf{H}_{pq,t} = \left(\mathbf{u}_{pq,t_c}, \ldots, \mathbf{u}_{pq,t_c}, \ldots, \mathbf{u}_{pq,t_c} \right)^T$.

Definition 1.2. (Frequency direction spacing) The vector of size n_v that model the spacing between the (u, v) coordinates and the centre (u, v) coordinate of a baseline (p, q) across the frequency direction is defined as

$$\mathbf{d}_v = \frac{||\mathbf{u}_{pq,t_c}||}{c} \cdot \left\{ \boldsymbol{v} - v_c \cdot \mathbf{g}_v \right\},$$

where $\mathbf{g}$ is a $n_v \times 1$ unity matrix. The weight of a (u, v) data point is considered as follow:

Definition 1.3. (Baseline dependent windowing function)

---

[2] The *distance* has also huge dependences on the baseline length and allow us to formally define the data weight of a uv point over the entire uv plane.

If f_{pq} is a *baseline dependent windowing function*, then:

$$f_{pq} : \{\mathcal{R}, \mathcal{R}\} \quad \rightarrow \quad \mathcal{R}$$
$$d_{t_i}, d_{v_j} \quad \mapsto \quad \frac{w_{t_i, v_j}}{\sum_{i=1}^{n_t} \sum_{j=1}^{n_v} w_{t_i, v_j}}.$$

where d_{t_i} is an element of the vector $\mathbf{d}_t = \overline{\overline{\mathbf{U}^s}}_{pq,t}$ and d_{v_j} is an element of the vector $\mathbf{d}_v$.

The previous algorithm is correct. But unfortunately, the algorithm does not suppressed out FoV sources and we loosed in sensitivity. Although simple averaging "means high sensitivity", we do need to eliminate at a certain rate out FoV sources in such a way that the overall SNR becomes higher than the one of averaging. We described such an algorithm in the following section.

4 DERIVATION OF BDWF: FOV SIGNALS RECOVERY AND OUT FOV SUPPRESSION

4.1 Description

In theory, windowing functions and signals generally extend to infinity. Unfortunately, in practice, filtering a signal with a low pass filter, one need to define a cut-off interval. Therefore, if one wants to achieve sufficiently an accurate estimate of the windowing function ideal spectrum, one need a wide cut-off interval as far as the spectrum approaches the ideal when the windowing function order increases. An overlap baseline dependent windowing function aims to extend the order of the baseline dependent windowing function in such a way that, we approaches the ideal spectrum. The only drawback of this technique is the increased of the time needed for processing the output sample of the signals being integrate.

4.2 Methods

The weight of a visibility is not defined by a unique baseline dependent windowing, but by the strength of the correlation between the overall overlapping baseline dependent windowing functions on the visibility. Now, consider that f_{pq}^a is an overlap-*BDWF* of width Δt and Δv across the time and frequency direction respectively.

Definition 1.4. (Left hand side overlapping functions) if $\Delta_l t$ and $\Delta_l v$ are the overlap time interval and frequency interval of the baseline dependent windowing function $f_{pq}^{a_0}$ respectively and $\left\{ f_{pq}^{a_1}, f_{pq}^{a_2}, f_{pq}^{a_3}, \dots \right\}$ the set of *BDWF* overlapping on the *left hand side* of $f_{pq}^{a_0}$ then the resulting *BDWF* within $\Delta_l t$ and $\Delta_l v$ is defined as

$$g_{pq}^{lhs} : \{\mathcal{R}, \mathcal{R}\} \quad \rightarrow \quad \mathcal{R}$$
$$d_{t_i}, d_{v_j} \quad \mapsto \quad \frac{1}{N_{lhs}} \left(\sum_k f_{pq,(d_{t_i}, d_{v_j})}^{a_k} + f_{pq,(d_{t_i}, d_{v_j})}^{a_0} \right).$$

Here, N_{lhs} is the normalization term defined as

$$N_{lhs} = \sum_{i=1}^{n_{lt}} \sum_{j=1}^{n_{lv}} \left(\sum_k f_{pq,(d_{t_i}, d_{v_j})}^{a_k} + f_{pq,(d_{t_i}, d_{v_j})}^{a_0} \right),$$

where n_{lt} and n_{lv} are the number of (u, v) coordinates

changes and frequency changes within $\Delta_l t$ and $\Delta_l v$ respectively.

Definition 1.5. (Right hand side overlapping functions) if $\Delta_r t$ and $\Delta_r v$ are the overlap time and frequency interval of a *BDWF* $f_{pq}^{a_0}$ respectively and $\left\{ f_{pq}^{a_1}, f_{pq}^{a_2}, f_{pq}^{a_3}, \dots \right\}$ the set of *BDWF* overlapping on the *right hand side* of $f_{pq}^{a_0}$, then the resulting *BDWF* within $\Delta_r t$ and $\Delta_r v$ is defined as

$$g_{pq}^{rhs} : \{\mathcal{R}, \mathcal{R}\} \quad \rightarrow \quad \mathcal{R}$$
$$d_{t_i}, d_{v_j} \quad \mapsto \quad \frac{1}{N_{rhs}} \left(f_{pq,(d_{t_i}, d_{v_j})}^{a_0} + \sum_k f_{pq,(d_{t_i}, d_{v_j})}^{a_k} \right).$$

Here, N_{rhs} is the normalization term defined as

$$N_{rhs} = \sum_{i=1}^{n_{rt}} \sum_{j=1}^{n_{rv}} \left(f_{pq,(d_{t_i}, d_{v_j})}^{a_0} + \sum_k f_{pq,(d_{t_i}, d_{v_j})}^{a_k} \right),$$

where n_{rt} and n_{rv} are the number of (u, v) coordinates changes and frequency changes within $\Delta_r t$ and $\Delta_r v$ respectively.

Definition 1.6. (Overlap baseline dependent windowing functions) If $f_{pq}^{a_0}$ is a baseline dependent windowing function defined within the time interval Δt and the frequency interval Δv, g_{pq}^{lhs} the result of the left hand side of $f_{pq}^{a_0}$ overlapping windowing functions within the time interval $\Delta_l t$ and the frequency interval $\Delta_l v$, and g_{pq}^{rhs} the result of the right hand side of $f_{pq}^{a_0}$ overlapping windowing functions within the time interval $\Delta_r t$ and the frequency interval $\Delta_r v$, then the overlap baseline dependent windowing function within Δt and Δv is defined as:

$$g_{pq} = \begin{cases} g_{pq}^{lhs} & \text{if } (t, v) \in (\Delta_l t, \Delta_l v) \\ f_{pq}^{a_0} & \text{if } (t, v) \in (\Delta_u t, \Delta_u v) \\ g_{pq}^{rhs} & \text{if } (t, v) \in (\Delta_r t, \Delta_r v) \end{cases}$$

From the above definitions, the following derivation is trivial

$$\left\{ \Delta t, \quad \Delta v \right\} = \left\{ \Delta_l t \cup \Delta_u t \cup \Delta_r t, \quad \Delta_l v \cup \Delta_u v \cup \Delta_r v \right\},$$

where $\Delta_u t$ and $\Delta_u v$ are $f_{pq}^{a_0}$ uncorrelated time and frequency interval respectively. They follows the below rules

$$\Delta_u t = \begin{cases} \cup \{t_i\}_{i=s', \ s' \geq s+1}^{c', \ c' \leq c-1} & \text{if } n_{lt} + n_{rt} < n_t \\ \{t_c\} & \text{if } n_{lt} + n_{rt} = n_t \\ \varnothing & \text{otherwise} \end{cases}$$

$$\Delta_u v = \begin{cases} \cup \{v_i\}_{i=s', \ s' \geq s+1}^{c', \ c' \leq c-1} & \text{if } n_{lv} + n_{rv} < n_v \\ \{v_c\} & \text{if } n_{lv} + n_{rv} = n_v \\ \varnothing & \text{otherwise} \end{cases}$$

4.3 Windowing functions

In signal processing a windowing function is a mathematical function that is zero-values outside of some chosen interval, and when another function or a signal is multiplied by the windowing function, the product is also zero-values outside the interval. In this section, we evaluation the Peak Sidelobe Level (PSL), the Main Lobe width (MLW) and the Sidelobes Roll-off (SLR) of some windowing functions spectrum. This study will allow us to make a suitable choice of the window
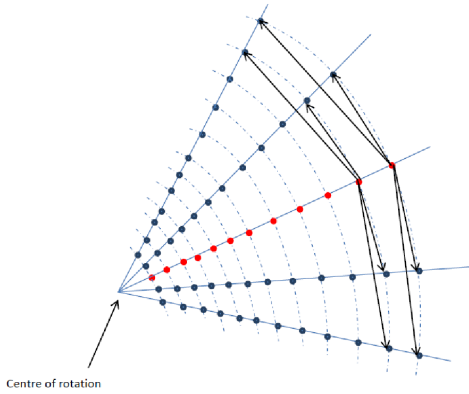
Figure 3. Snapshot coverage

Figure 4. *Bl-sincw*1 used to convolve the visibility data obtained from the long, medium and short baseline

that by tapering with the sky, we conserve the brightness of sources in the field of interest and attenuate sidelobes confusion from strong sources out of the field of interest.

4.3.1   Boxcar window: natural weighting

This windowing function take a hunk of the data without modification, and this leads to discontinuities at the edges[3]. For a cut-off frequency interval $[-v_a, v_a]$ the boxcar windowing function is defined as:

$$\Pi_u = \begin{cases} 1 & -v_a \leqslant v \leqslant v_a \\ 0 & \text{otherwise} \end{cases} \quad (13)$$

Fig.5 and Fig.6 gives the graph of Π_u and its spectrum respectively. The blue and the red curve of Fig.6 are the spectrum of Π_u for a frequency cut-off interval, $[-v_a, v_a]$ and $[-v_a/2, v_a/2]$ respectively. We noticed that when the cut-off interval is large, the MLW of the spectrum is narrower, the PSL is lower and the SLR drop faster.

4.3.2   Gaussian window

A Gaussian windowing function centred at mean zero with standard deviation, σ can be described as

$$G_u = e^{-bv^2}. \quad (14)$$

Here, $b = (2\sigma^2)^{-1}$ and $\mathcal{F}^{-1}\{G_u\} = \sqrt{\frac{b}{\pi}}e^{-cl^2}$, where $c = \pi^2/b$. This shows us that the inverse Fourier transform of a Gaussian with standard deviation σ is a Gaussian with a standard deviation $\sigma' = (2\pi\sigma)^{-1}$.

Fig.11 and Fig.12 gives the graph of G_u and its spectrum respectively, where G_u is truncate within the cut-off frequency interval $[-v_a, v_a]$, with $b = 3$ for the blue curve and $b = 5$ for the red one. We noticed that when the standard deviation is large, the MLW of the spectrum is narrower, the PSL is higher and the SLR drop slowly compare to a smaller standard deviation.

4.3.3   Butterworth

The frequency response of the Butterworth filter is flat in the pass band, and rolls off towards zero in the stop band, and it is characterized by two independent parameters, the cut-off frequency v_a and the order p. These two parameters controls the bandwidth and side lobes attenuation. The frequency response of the Butterworth is given by

$$B_u = \left(1 + (v/v_a)^{2p}\right)^{-1}. \quad (15)$$

For the same frequency interval $[-v_a, v_a]$, we plotted three curves $\{p = 1, p = 3, p = 5\}$ of B_u in Fig.9 and their corresponding spectrum in Fig.10. We noticed that when the other p is getting bigger, the MLW of the spectrum is conserved, while the PSL is getting higher and the SLR is dropping faster.

4.3.4   Bessel Function of the First Kind

4.3.5   First order prolate spheroidal wave function

4.3.6   Sinc window

In theory, the sinc window is an infinitely large convolution filter as it is non zero everywhere, and its inverse Fourier Transform produces the ideal filter kernel (the boxcar windowing function). The sinc is defined as follow:

$$S_u = sinc\left(\pi bu(t/\lambda_a)\right). \quad (16)$$

However, in practice some one need to defined a cut-off interval where the window is considered to be non zero, and zero out of this cut-off interval. Fig.7 and Fig.8 gives the graph of S_u and its spectrum respectively, where S_u is truncate within the cut-off frequency interval $[-v_a, v_a]$. We noticed that when the cut-off frequency interval is large (Fig.8, blue curve), the spectrum becomes perfectly flat at the passband while the MLW becomes narrower, the PSL becomes lower and the SLR drop faster compare to a cut-off frequency of $[-v_a, v_a]$ (Fig.8, red curve).

---

[3] unless it happens that the signal fit exactly with the windowing function width. Nevertheless, it is rare to find such a situation.

Windows	MLL (-3db)	PSL (db)	SLR (db/octave)
Π_u	$\approx 0,073$	$-6,68$	$-6,78$
$\mathcal{F}^{-1}\{\Pi_u\}$	$\approx 0,306$	$-11,22$	$-12,42$
G_u	$\approx 0,0736$	$-30,28$	$-14,5$
B_u	$\approx 0,079$	$-10,08$	$-15,39$
P_u	$\approx -$	$-$	$-$

A windowing function with a narrower main lobe width for a better spectral resolution, lower PSL to have less masking of nearby sources, and faster SLR to have less masking for far away sources is preferably in this work. Nevertheless, The energy is more concentrated in the frequency domain main lobe when the lobe width is narrower. Therefore, the frequency domain of the boxcar and the Butterworth window look similar, but the other of the Butterworth frequency domain can be control with the goal to concentrate more energy in the frequency main lobe. However, the sinc window is preferable as we expect in this work, signals in a wide dynamic range.

4.3.7 Noise and comparison

The methods described in section (3) and section (4) are use in this subsection to evaluate the theoretical noise, f_{pq} and g_{pq} are replaced in Eq.**??** and Eq.**??** respectively by the windowing functions described above. Table (4.3.7) and (4.3.7) summarize the theoretical noise where these functions are used as a baseline dependent windowing and as an overlap baseline dependent windowing functions respectively.

f_{pq}	Theoretical noise	g_{pq}	Theoretical noise
Π_u	1,066	Π_u	1,066
$\mathcal{F}^{-1}\{\Pi_u\}$	1,066	$\mathcal{F}^{-1}\{\Pi_u\}$	1,066
G_u	1,334	G_u	1,334
B_u	1,066	B_u	1,066
$\mathcal{F}^{-1}\{B_u\}$	1,066	$\mathcal{F}^{-1}\{B_u\}$	1,066
P_u	1,334	P_u	1,334

1.) In Figure 1.) In Figures (**??**) and (**??**) we represented the ratio $\frac{\sigma_{meas,pq}}{\sigma_{av,pq}}$ as a function of $\sum_i^n u_i((t_c - t_i)/\lambda))$ ($\sigma_{meas,pq}, \sigma_{av,pq}$ are the per baselines CWF and averaging rms noise respectively). We could also represented it as a function of baseline length. But, a uv-track corresponding to baseline aligned along the Est-West direction has longer tracts compare to one aligned along the South-Nordth for the same integration and frequency band. Therefore, $\frac{\sigma_{meas,pq}}{\sigma_{av,pq}}$ v/s baselines length is ambiguous. We consider five baselines dependent windowing sinc function, *Bl-sinc wk* (with an extended width of $(k-1)n$ time intervals and/or frequency channels and $k \geqslant 1$). The experiment is done for two cases, figure (**??**) is the one for *Bl-sinc wk* over both time-frequency and figure (**??**) over time. These figures shows that, the noise increases with baselines length.

2.) Figure (**??**) shows that, with *Bl-sinc wk*, the noise is lower on shorter baselines compared to the longer baselines. This is because on shorter baselines $\frac{\sigma_{meas,pq}}{\sigma_{av,pq}} \approx \frac{n}{n+k}$, it is the same

case with Figure (**??**) where $\frac{\sigma_{meas,pq}}{\sigma_{av,pq}} \approx \sqrt{\frac{n}{n+k}}$ (see the proof). With *Bl-Sinc wk* ($k > 1$), the noise drops with the extended number of time intervals and/or frequency channels of the window. The rate of this drop is non-linear with baselines length and also with the overlap time interval and/or frequency channels (see figure (**??**b) and (**??**b), the variation of the noise rate between baselines).

3.) In spite of the overlapping, with the theoretical results, the noise of longer baselines do not drop when the overlap samples is increased (figure **??**). The reason is, few windows are overlapping in a visibility point when we extended in a unique direction (the time interval in this case) compare to two directions (time interval and frequency channels). The theoretical derivation for the overall noise of *Bl-sinc wk* and the simulated one are quantified similarly but the pattern of the per baseline simulated rms noise do not look the same with the theoretical one. The number of k determines the amount of noise of CWF.

5 SIMULATIONS AND RESULTS

In order to test the algorithms described in section and section, we performed multiple tests on JVLA simulated measurement sets (MS). In this section we summarize and discussed those results. Several windowing functions were described in the previous section, the sinc window and the Bessel of the first kind approaches well our specifications, and they are taken under consideration. Two MS is used in our simulation, a high resolution MS (HR-MS) that contained the observed JVLA data of short integration time and frequency, a low resolution MS (LR-MS), where the simple averaged or the weight averaged data are saved. To apply the second algorithm described in section 4, the following conditions are satisfied:

(i) If t_{start}^{hrms} and t_{start}^{lrms} are the starting time of the HR-MS and LR-MS respectively. $n_{t,ovlp}$ the number of timeslots extended across the time direction, and Δt^{hrms} the HR-MS integration time, then $t_{start}^{lrms} \geqslant t_{start}^{hrms} + n_{t,ovlp} \times \Delta t^{hrms}$.

(ii) If t_{end}^{hrms} and t_{end}^{lrms} are the ending time of the HR-MS and LR-MS respectively, then $t_{end}^{lrms} \leqslant t_{end}^{hrms} + n_{t,ovlp} \times \Delta t^{hrms}$.

(iii) If ν_{start}^{hrms} and ν_{start}^{lrms} are the starting frequency of the HR-MS and LR-MS respectively. $n_{\nu,ovlp}$ the number of channels extended across the frequency direction, and $\Delta \nu^{hrms}$ the HR-MS width, then $\nu_{start}^{lrms} \geqslant \nu_{start}^{hrms} + n_{\nu,ovlp} \times \Delta \nu^{hrms}$.

(iv) If ν_{end}^{hrms} and ν_{end}^{lrms} are the ending frequency of the HR-MS and LR-MS respectively, then $\nu_{end}^{lrms} \leqslant \nu_{end}^{hrms} + n_{\nu,ovlp} \times \Delta \nu^{hrms}$.

### 5.1 Smearing elimination and out FoV suppression

We considered 40 sky models of 1Jy source, the sky models differ from each other by the source coordinates. However, the reason of having a unique source in the sky model is to avoid interferences that can cost calibration artefacts in the sky maps (T. L. Grobler et al. 2014) which can affect the brightness of these sources. Another obvious effect is the CLEAN algorithm (T. L. Grobler et al. 2014) that does not clean the dirty map at 100%, therefore we need to avoid flux distribution between sources
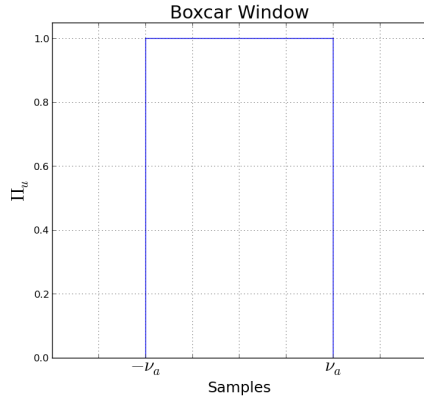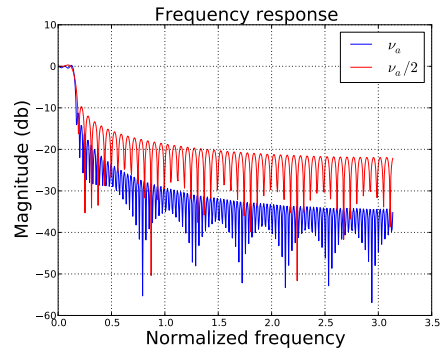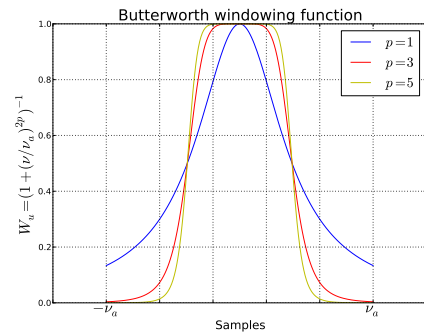
Figure 5. Boxcar windowing function.
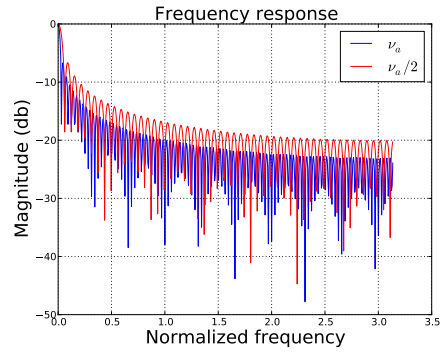
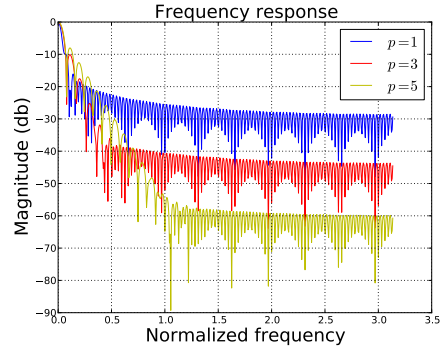**Figure 6.** Overlap *BDWF's*: $\Delta_u t = [225, 250]$.
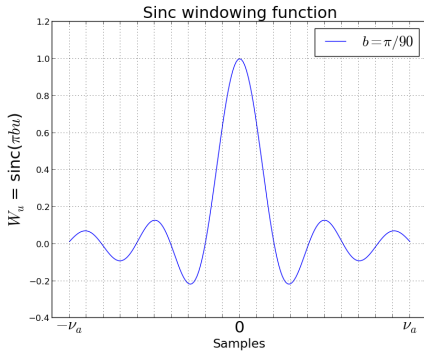
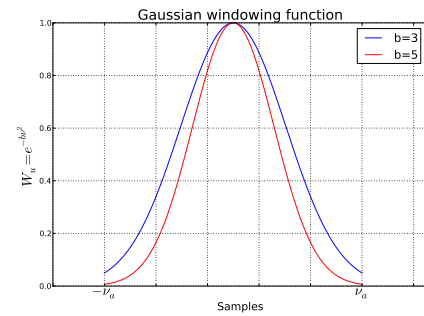

Figure 7. Overlap *BDWF's*: $\Delta_u t = \{250\}$.
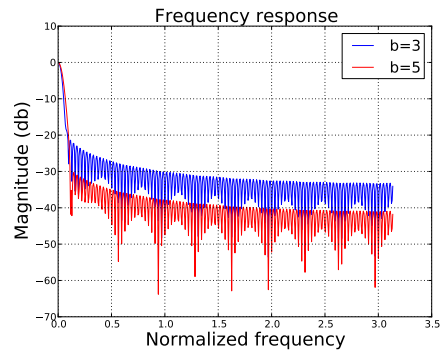

Figure 8. Overlap *BDWF's*: $\Delta_u t = \varnothing$.

Figure 9. Overlap *BDWF's*: $\Delta_u t = \{250\}$.
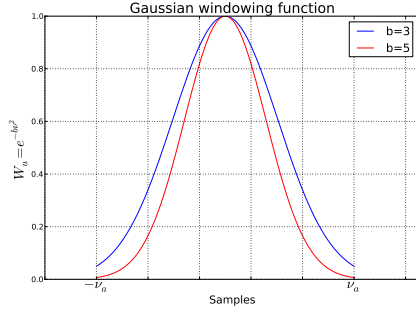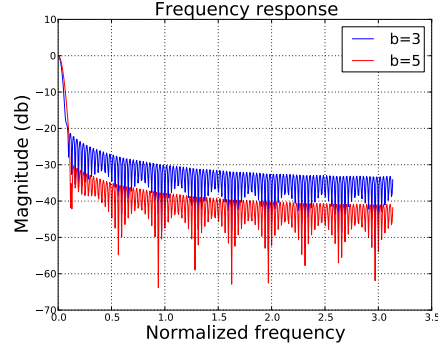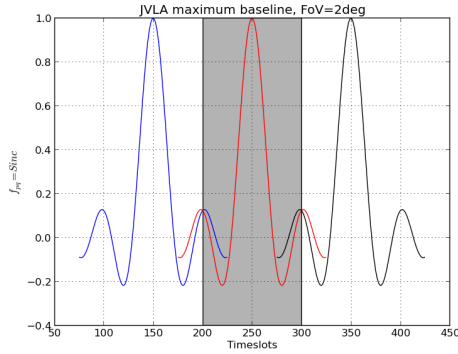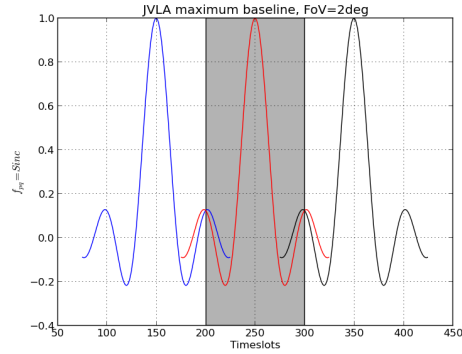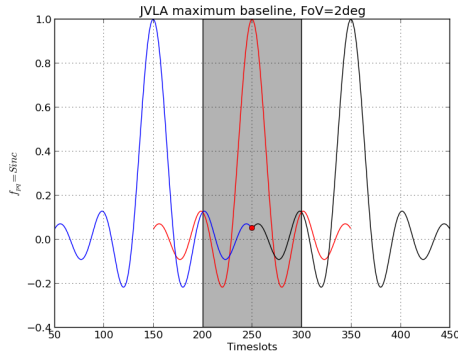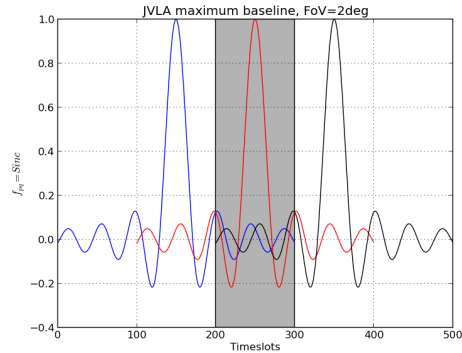

Figure 10. Overlap *BDWF's*: $\Delta_u t = \varnothing$.

Figure 11. Overlap *BDWF's*: $\Delta_u t = \{250\}$.

Figure 12. Overlap *BDWF's*: $\Delta_u t = \varnothing$.

Figure 13. Overlap *BDWF's*: $\Delta_u t = \{250\}$.

Figure 14. Overlap *BDWF's*: $\Delta_u t = \varnothing$.

Figure 15. Overlap *BDWF's*: $\Delta_u t = [225, 250]$.

Figure 16. Overlap *BDWF's*: $\Delta_u t = [225, 250]$.

Figure 17. Overlap *BDWF's*: $\Delta_u t = \{250\}$.

Figure 18. Overlap *BDWF's*: $\Delta_u t = \varnothing$.

via their sidelobes. Each of the sky model is simulated with a JVLA HR-MS of 7min30s snapshot synthesis, with a $\Delta t^{hrms} = 1.5s$ integration time at 1.4GHz, with 150 channels of width Δv^{hrms}=125kHz. We therefore applied the actual method (simple averaging) and our methods, each result is save into a LR-MS of 1min30s synthesis, with a 150s integration time, with 1 channels of width 6.25MHz. We considered, $\{t_{start}^{hrms}, v_{start}^{hrms}\} = \{0s, 125kHz\}$, $\{t_{start}^{lrms}, v_{start}^{lrms}\} = \{1min30s, 6250kHz\}$, $\{t_{end}^{hrms}, v_{end}^{hrms}\} = \{7min30s, xxxkHz\}$, $\{t_{end}^{lrms}, v_{end}^{lrms}\} = \{6min, xxxkHz\}$, $n_{t,ovlp} = \{0, 100, 150\}$ and $n_{v,ovlp} = \{0, 25, 50\}$.
Fig.B3, Fig.B4, Fig.B5 and Fig.B6 show the results of the simulation, where we represented the brightness of the source

as a function of the source coordinates in the sky model. In these figures, we considered three cases of the sinc window, and three of the Bessel first kind (*Bl-sinc* $Wn_{t,ovlp} \times n_{v,ovlp}$, *Bl-J$_0$* $Wn_{t,ovlp} \times n_{v,ovlp}$ with $n_{t,ovlp} = \{0, 100, 150\}$ and $n_{v,ovlp} = \{0, 25, 50\}$). We evaluated the loss in signal amplitude with longer LR-MS integration time interval $\Delta t^{lrms} = 150s$ and wider LR-MS integration frequency interval $\Delta v^{lrms} = 6250kHz$. We furthermore evaluated the noise ratio, $\mathcal{R}_\sigma = \frac{\sigma_w}{\sigma_{Avg}}$ (with σ_w the resulting noise of the filter under consideration and σ_{Avg} the noise of simple averaging). These results shows that:

• We measured more than 90% of the source brightness within $\approx$ 75% of the FoV using *Bl-sinc* $W0 \times 0$ and *Bl-J$_0$*

$W0 \times 0$. Unfortunately, the attenuation rate of the source out of the FoV is approximately the same when performing with simple averaging.

• We measured more than 90% of the source brightness within $\approx$ 95% of the FoV with the overlap filters. However, as mention in section 4.3 the reason for this is that, the overlap filter is an accurate practical evaluation of the window theoretical representation[4].

• Another obvious effect of the overlap filters is the suppression of the source when this source is out of the FoV. When looking at these figures, it appears that the curves of the overlaps filters are below the one of simple averaging. However, the overlaps filters attenuated $\approx$ 99% of the source brightness out of the FoV.

• When looking at these figures, it appears that the sinc window conserved the signal within the FoV compared to the Bessel of the first kind window, while the Bessel of the first kind suppressed the signal out of the FoV compare to the sinc. However, the reason for this is that the main lobe width of the sinc is narrower than the one of the Bessel first kind and the Bessel first kind has low sidelobes level compared to the sinc.

When performing the baseline dependent filters, smearing is eliminated within the FoV while we compressed the data by integrating over a large time interval and wider frequency interval of a LR-MS. However, under some assumptions, the overlap baseline dependent filters significantly attenuate the source out of the FoV to a greater extent than simple averaging. Thus, in all cases the SNR obtained using these methods are greater than the one using the simple averaging method even as there is loss in sensitivity.

5.2   Maximal integration

In this section, the maximal frequency and time integration that can be consider in the frequency direction and the time direction without smearing in the FoV while the methods accurately suppressed the source when this is out of the FoV is evaluated. However, we considered 6 sky models of a 1Jy source with different coordinates ($r = \{0.09°, 0.25°, 0.5°, 1°, 1.5°, 2°\}$). The methods are performed with a 2° FoV sinc and Bessel first kind filters centered in the phase centre.

5.2.1   Frequency direction

In this case, each of these sky model is simulated with a JVLA HR-MS of 1 timeslots synthesis, with a short integration time of $\Delta t^{hrms} = 0.1s$ at 1.4GHz. The aims of a short HR-MS integration time is to avoid time direction smearing and therefore accurately evaluate smearing in the frequency direction. We considered 150 channels, and varied the width, $\Delta \nu^{hrms}$ in the interval $[125, 1187.5]$ kHz. We therefore applied the actual method (simple averaging) and our methods both in the frequency direction, each result is save into a LR-MS of 1 timeslot synthesis, with 0.1s integration time and 1 channels of width $\Delta \nu^{hrms} \times 50$ kHz. We considered, $\nu^{hrms}_{start} = \Delta \nu^{hrms} kHz$, $\nu^{lrms}_{start} = \nu^{hrms}_{start} \times 50kHz$,

$\nu^{hrms}_{end} = \nu^{hrms}_{start} \times 150kHz$ and $\nu^{lrms}_{end} = \nu^{lrms}_{start} \times 100kHz$.

We compared in Fig.B7 and Fig.B8 the results of simple frequency averaging and the one of *Bl-sinc* $Wn_{\nu,ovlp}$ performed in the frequency direction. We compared in Fig.B9 and Fig.B10 the results of simple frequency averaging and the one of *Bl*-J_0 $Wn_{\nu,ovlp}$. Here we took $n_{\nu,ovlp} = \{0, 50\}$ frequency overlap bins. These results shows that:

• Firstly, these results show that, we can significantly integrate over a wider LR-MS frequency interval without a lost of signal amplitude. However, looking at these figures, the curves of the source at $0.09°, 0.25°, 0.5°$ from the phase centre are closer to the affine equation $y = 1$, which differ from the curves when the source is at $1°, 1.5°, 2°$ from the phase centre.

• Secondly, looking on Fig.B8 and B10, when the source is at $1.5°$ and $2°$, the attenuation is significant within $[6.2, 12.6] MHz$ with the overlap frequency direction filters compare to simple frequency averaging.

• Finally, the sinc filter performed well on signal recovery compare to the Bessel first kind and the Bessel first kind suppressed the source when this is out of the FoV compare to the sinc.

5.2.2   Time direction

In this case, each of these sky model is simulated with a JVLA HR-MS of 300 timeslots synthesis, and we varied the integration time Δt^{hrms} in the interval $[0.5, 5.5]s$ at 1.4GHz. We considered 1 channels of width, $\Delta \nu^{hrms} = 125kHz$. We therefore applied the actual method (simple averaging) and our methods both in the time direction then the result of each simulation is saved into a LR-MS of $100 \times \Delta t^{hrms} s$ synthesis, with a $100 \times \Delta t^{hrms} s$ integration time, with 1 channels of width 125kHz. We considered, $t^{hrms}_{start} = 0s$, $t^{lrms}_{start} = 100 timeslots \times \Delta t^{hrms} s$, $t^{hrms}_{end} = 300 timeslots \times \Delta t^{hrms} s$ and $t^{lrms}_{end} = 200 timeslots \times \Delta t^{hrms} s$.

We compared in Fig.B11 and Fig.B12 the results of simple time averaging and the one of *Bl-sinc* $Wn_{t,ovlp}$ performed in the time direction. We compared in Fig.B13 and Fig.B14 the results of simple time averaging and the one of *Bl*-J_0 $Wn_{t,ovlp}$. Here, we took $n_{t,ovlp} = \{0, 100\}$ time overlap bins. These results shows that:

• Firstly, we can significantly integrate over a longer LR-MS time interval without a lost of signal amplitude. However, looking at these figures, the curves of the source at $0.09°, 0.25°, 0.5°$ from the phase centre are closer to the affine equation $y = 1$, which differ from the curves when the source is at $1°, 1.5°, 2°$ from the phase centre.

• Secondly, looking on Fig.B8 and B10, when the source is at $1.5°$ and $2°$, the attenuation is significant within $[50, 150]$ with the overlap time direction filters compare to simple time averaging.

• Finally, the sinc filter performed well on signal recovery compare to the Bessel first kind and the Bessel first kind suppressed the source when this is out of the FoV compare to the sinc.

5.2.3   Time and frequency direction

In this case, each sky model is simulated with a JVLA HR-MS of 300 timeslots synthesis, and varied the inte-

---

[4] windowing function theoretically extend to infinitely

gration time Δt^{hrms} in $[0.5, 5.5]s$ at $1.4GHz$. We considered 150 channels and varied the width $\Delta \nu^{hrms}$ within the interval $[125., 750.]kHz$. We therefore applied the actual method (simple averaging) and our methods both in the frequency direction and time direction, each result is save into a LR-MS of 100timeslots$\times \Delta t^{hrms}s$ synthesis, with 100timeslots$\times \Delta t^{hrms}$ integration time and 1 channels of width 50channels$\times \Delta \nu^{hrms}kHz$. We considered, $t_{start}^{hrms} = 0s$, $t_{start}^{lrms} = 100$timeslots$\times \Delta t^{hrms}s$, $t_{end}^{hrms} = 300$timeslots$\times \Delta t^{hrms}s$ and $t_{end}^{lrms} = 200$timeslots$\times \Delta t^{hrms}s$, $\nu_{start}^{hrms} = \Delta \nu^{hrms}kHz$, $\nu_{start}^{lrms} = \nu_{start}^{hrms} \times 50kHz$, $\nu_{end}^{hrms} = \nu_{start}^{hrms} \times 150kHz$ and $\nu_{end}^{lrms} = \nu_{start}^{hrms} \times 100kHz$.

We compared in Fig.B15 and Fig.B16 the results of simple time and frequency averaging and the one of *Bl-sinc* $Wn_{t,ovlp} \times n_{\nu,ovlp}$ performed in the time and frequency direction. We compared in Fig.B17 and Fig.B18 the results of simple time and frequency averaging and the one of *Bl-*J_0 $Wn_{t,ovlp} \times n_{\nu,ovlp}$ performed in the time and frequency direction. Here, we took $n_{t,ovlp} = \{0, 100\}$ time overlap bins and $n_{\nu,ovlp} = \{0, 50\}$ frequency overlap bins. These results shows that:

• Firstly, we can significantly integrate over a longer LR-MS time interval and frequency interval at the same time without a lost of signal amplitude. However, looking at these figures, the curves of the source at $0.09°, 0.25°, 0.5°$ from the phase centre are closer to the affine equation $y = 1$, which differ from the curves when the source is at $1°, 1.5°, 2°$ from the phase centre.

• Secondly, looking on Fig.B16 and B18, when the source is at $1.5°$ and $2°$, it appears that the curves of the overlaps filters are below the one of simple averaging. These suggest that, when we are integrating both over a wider LR-MS time interval and frequency interval, the source is suppressed significantly out of the FoV without any constraint on the integration time and frequency.

• Finally, the sinc filter performed well on signal recovery compare to the Bessel first kind and the Bessel first kind suppressed the source when this is out of the FoV compare to the sinc.

5.3 Multiple sources in the sky model and attenuation efficiency

5.4 Discussion

6 CONCLUSIONS

The goal of this paper was threefold. The first objective was to investigate **** windowing functions***
The second objective was to study ****first algorithm data compression***
The final objective was to ****second algorithm data compression and out field suppression***
Drawback and futures works*** drawback and futures works*****

REFERENCES

Linfield R., 1986, AJ, 92, 213

Martí-Vidal I., Marcaide J., 2008, A&A, 480, 289
T. L. Grobler C. D. N., O. M. Smirnov A. J. v. Z., van Zyl A. J., 2014, A&A, 480, 4

APPENDIX A: DERIVATION OF COMPLEX MATRICES

The complex matrices used in section 2.4 are explicitly derived in this appendix. In Eq.7, the matrices $\mathbf{C}_{(t,\nu)}^{block}$ and $\mathbf{W}_{pq,(t,\nu)}^{block}$ are blocks diagonals both of size $(4n_t n_\nu) \times (4n_t n_\nu)$, and the sampled visibilities $\mathbf{V}_{pq,(t,\nu)}^{samp}$ is a vector of size $4 \times (n_t n_\nu)$. These matrices are explicitly expressed as follow:

$$\mathbf{C}_{(t,\nu)}^{block} = \begin{bmatrix} \mathbf{c}_{(t,\nu)} & 0 & 0 & 0 \\ 0 & \mathbf{c}_{(t,\nu)} & 0 & 0 \\ 0 & 0 & \mathbf{c}_{(t,\nu)} & 0 \\ 0 & 0 & 0 & \mathbf{c}_{(t,\nu)} \end{bmatrix}$$

$$\mathbf{W}_{pq,(t,\nu)}^{block} = \begin{bmatrix} \mathbf{W}_{pq,(t,\nu)} & 0 & 0 & 0 \\ 0 & \mathbf{W}_{pq,(t,\nu)} & 0 & 0 \\ 0 & 0 & \mathbf{W}_{pq,(t,\nu)} & 0 \\ 0 & 0 & 0 & \mathbf{W}_{pq,(t,\nu)} \end{bmatrix}$$

$$\mathbf{V}_{pq,(t,\nu)}^{samp} = \begin{bmatrix} \mathcal{V}_{pq,(t,\nu)}^0, \mathcal{V}_{pq,(t,\nu)}^1, \mathcal{V}_{pq,(t,\nu)}^2, \mathcal{V}_{pq,(t,\nu)}^3 \end{bmatrix}^T.$$

In Eq.**??**, the matrices $\mathbf{C}_{(t,\nu)}^{block,n}$ and $\mathbf{W}_{pq,(t,\nu)}^{block,n}$ are blocks diagonals both of size $(4N_\nu^{pq} n_t n_\nu) \times (4N_\nu^{pq} n_t n_\nu)$, and the sampled visibilities $\mathbf{V}_{pq,(t,\nu)}^{samp,n}$ is a one row matrix of size $(N_\nu^{pq} 4n_t n_\nu) \times (4n_t n_\nu)$ made of $\mathbf{V}_{pq,(t,\nu)}^{samp}$. These matrices are explicitly expressed as follow:

$$\mathbf{C}_{(t,\nu)}^{block,n} = \begin{bmatrix} \mathbf{C}_{(t,\nu)}^{block} & \cdots & 0 & \cdots & 0 \\ \vdots & \vdots & \vdots & \vdots & \vdots \\ 0 & \cdots & \mathbf{C}_{(t,\nu)}^{block} & \cdots & 0 \\ \vdots & \vdots & \vdots & \vdots & \vdots \\ 0 & \cdots & 0 & \cdots & \mathbf{C}_{(t,\nu)}^{block} \end{bmatrix}$$

$$\mathbf{W}_{pq,(t,\nu)}^{block,n} = \begin{bmatrix} \mathbf{W}_{pq,(t,\nu)}^{block} & \cdots & 0 & \cdots & 0 \\ \vdots & \vdots & \vdots & \vdots & \vdots \\ 0 & \cdots & \mathbf{W}_{pq,(t,\nu)}^{block} & \cdots & 0 \\ \vdots & \vdots & \vdots & \vdots & \vdots \\ 0 & \cdots & 0 & \cdots & \mathbf{W}_{pq,(t,\nu)}^{block} \end{bmatrix}$$

$$\mathbf{V}_{pq,(t,\nu)}^{samp,n} = \begin{bmatrix} \mathbf{V}_{pq,(t,\nu)}^{samp}, \cdots, \mathbf{V}_{pq,(t,\nu)}^{samp}, \cdots, \mathbf{V}_{pq,(t,\nu)}^{samp} \end{bmatrix}^T.$$

In Eq.10, the matrix $\mathbf{A}$ of size $(4N_v) \times (4N_{pix})$ is defined as follow

$$
\mathbf{A} = \begin{bmatrix}
\mathbf{C}_{(t,v)}^{block,n} \cdot \mathbf{W}_{01,(t,v)}^{block,n} \cdot \mathbf{S}_{01,(t,v)}^{block,n} \cdot \mathbf{F} \\
\vdots \\
\mathbf{C}_{(t,v)}^{block,n} \cdot \mathbf{W}_{ik,(t,v)}^{block,n} \cdot \mathbf{S}_{ik,(t,v)}^{block,n} \cdot \mathbf{F} \\
\vdots \\
\mathbf{C}_{(t,v)}^{block,n} \cdot \mathbf{W}_{jl,(t,v)}^{block,n} \cdot \mathbf{S}_{jl,(t,v)}^{block,n} \cdot \mathbf{F}
\end{bmatrix}
$$

APPENDIX B: SIMILAR WAY OF IMAGING

Each baseline has his own baseline dependent windowing functions during integration. Unfortunately, we can not accurately estimate the resulting spectrum of all windowing functions that multiply the sky seen by these baselines (if we supposed that all baselines are seen the same sky). The measured sky intensity of the array is derived from the inverse Fourier transform of the sum of the sample visibilities measured at each baseline. The mathematics behind this is as follow:

$$
\mathcal{I}_{l,m}^{D} = \mathcal{F}^{-1}\left\{ \sum_{pq} \mathcal{S}_{pq} \cdot \left(c_{pq} \cdot (\mathcal{W}_{pq} \circ \mathcal{V}) \right)_{(t,v)} \right\}
$$

where $\mathcal{S}_{pq}$ is the sampling function of the baseline pq. This can be rewritten as

$$
\mathcal{I}_{l,m}^{D} = \sum_{pq} \mathcal{B}_{pq} \circ \left(\mathcal{F}^{-1}\{c\}_{pq} \circ (\mathcal{R}_{pq} \cdot \mathcal{I}^{sky}) \right)_{(l,m)}
$$

Here, $\mathcal{R}_{pq} = \mathcal{W}_{pq}$ is the sky response or smearing response for the baseline pq. The same sky seen by all baselines is $\mathcal{I}^{sky}$ and $\mathcal{B}_{pq}$ is the synthesized beam or point spread function of the baseline pq. $\left(\mathcal{F}^{-1}\{c\}_{pq} \circ (\mathcal{R}_{pq} \cdot \mathcal{I}^{sky}) \right)_{(l,m)} = (\mathcal{R}_{pq} \cdot \mathcal{I}^{sky})_{(l,m)}$. Therefore, the dirty beam can be written as:

$$
\mathcal{I}_{l,m}^{D} = \left(\sum_{pq} \mathcal{B}_{pq} \circ \left(\mathcal{R}_{pq} \cdot \mathcal{I} \right) \right)_{(l,m)}
$$

If the integration windowing function were the same in all baseline, then we can write:

$$
\mathcal{I}_{l,m}^{D} = \left(\left(\sum_{pq} \mathcal{B}_{pq} \right) \circ \left(\mathcal{R} \cdot \mathcal{I} \right) \right)_{(l,m)}
$$

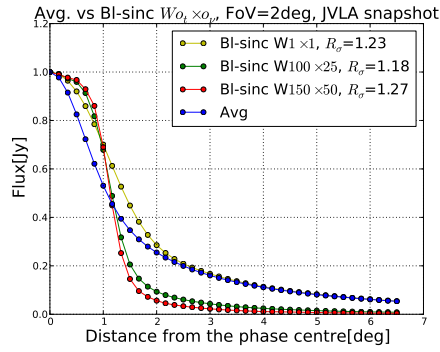This paper has been typeset from a TeX/ LaTeX file prepared by the author.
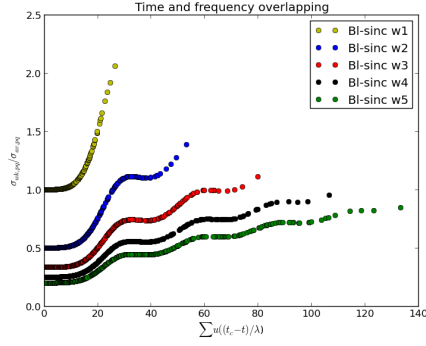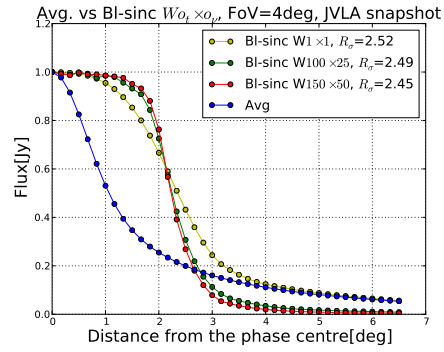
Figure B1. Noise ratio and rate of *Bl-sinc-wk*: time interval and frequency channels.
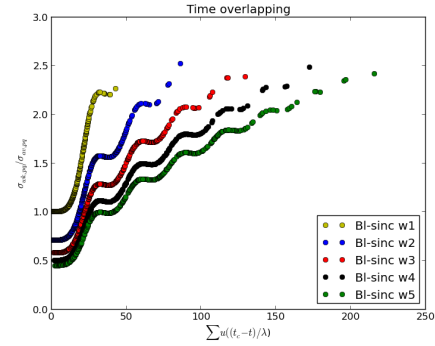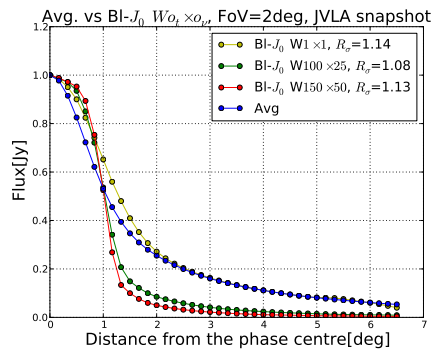
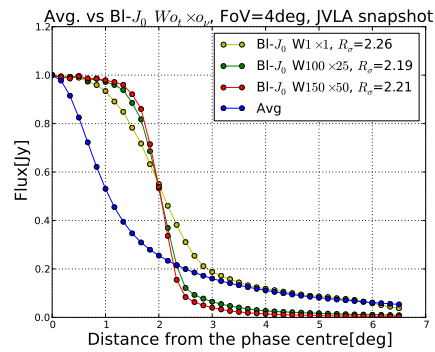**Figure B2.** Noise ratio and rate of *Bl-sinc-wk*: time interval.

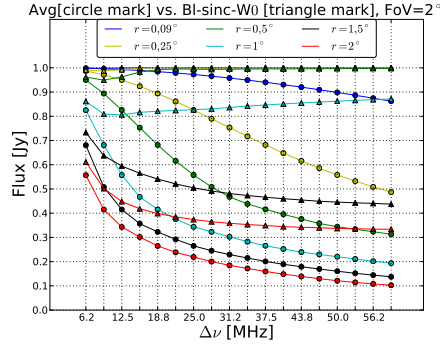**Figure B3.** Overlap *BDWF's*: $\Delta_u t = [225, 250]$.

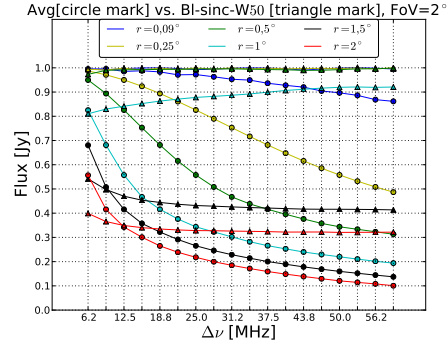**Figure B4.** Overlap *BDWF's*: $\Delta_u t = [225, 250]$.
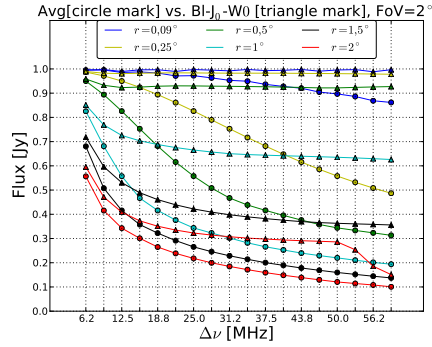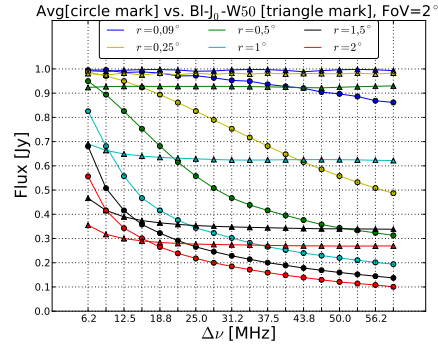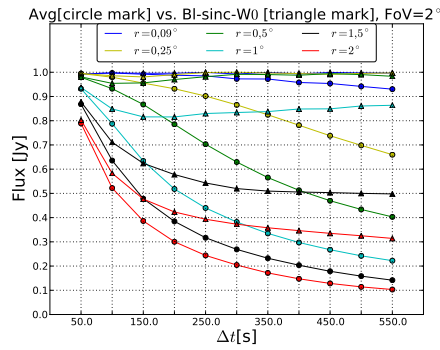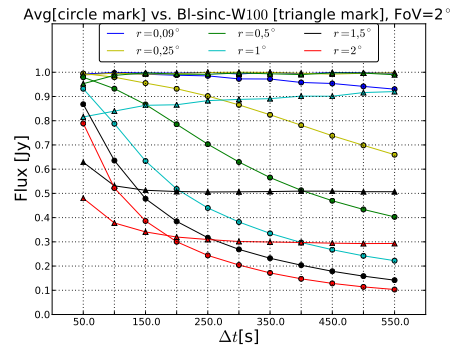

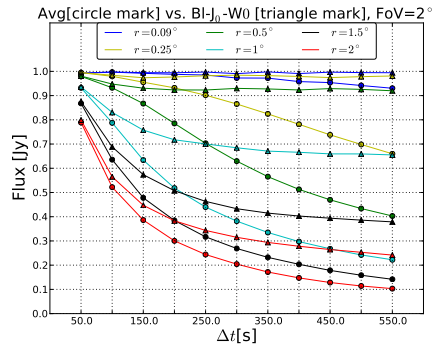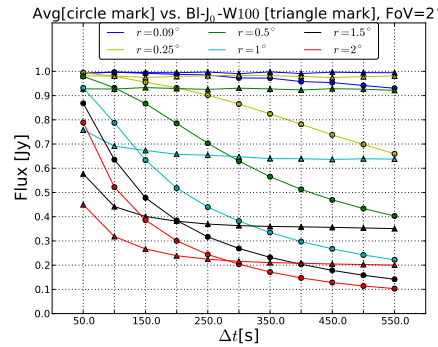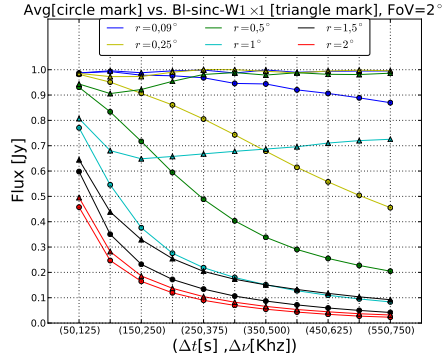**Figure B5.** Overlap *BDWF's*: $\Delta_u t = \{250\}$.

Figure B6. Overlap *BDWF's*: $\Delta_u t = \varnothing$.

Figure B7. Overlap *BDWF's*: $\Delta_u t = [225, 250]$.
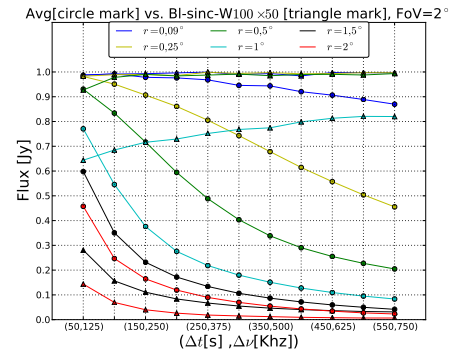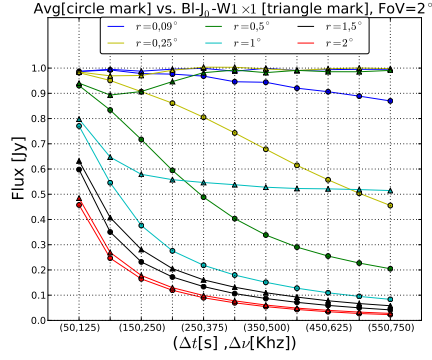

Figure B8. Overlap *BDWF's*: $\Delta_u t = [225, 250]$.

Figure B9. Overlap *BDWF's*: $\Delta_u t = \{250\}$.

Figure B10. Overlap *BDWF's*: $\Delta_u t = \varnothing$.

Figure B11. Overlap *BDWF's*: $\Delta_u t = [225, 250]$.
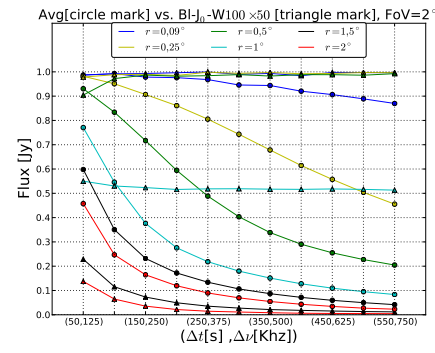

Figure B12. Overlap *BDWF's*: $\Delta_u t = [225, 250]$.

Figure B13. Overlap *BDWF's*: $\Delta_u t = \{250\}$.

Figure B14. Overlap *BDWF's*: $\Delta_u t = \varnothing$.

Figure B15. Overlap *BDWF's*: $\Delta_u t = [225, 250]$.

Figure B16. Overlap *BDWF's*: $\Delta_u t = [225, 250]$.

Figure B17. Overlap *BDWF's*: $\Delta_u t = \{250\}$.

Figure B18. Overlap *BDWF's*: $\Delta_u t = \varnothing$.